Differential cross section for proton-proton bremsstrahlung at 1.38 GeV/c

B. M. K. Nefkens and O. R. Sander*
Department of Physics, University of California, Los Angeles, California 90024

D. I. Sober
Department of Physics, University of California, Los Angeles, California 90024
and Department of Physics, The Catholic University of America, Washington, D. C.† 20064

H. W. Fearing
TRIUMF, Vancouver, British Columbia, Canada V6T 1W5

(Received 14 August 1978)

We present the differential cross section for proton-proton bremsstrahlung at an incident beam momentum of 1.38 GeV/c (730 MeV). The measurements are made with an overconstrained detection system to reliably exclude all $pp \to pp\pi^0$ events. We have obtained differential cross sections at 16 photon angles at photon energies up to 200 MeV for protons scattered at 50° (lab). For each of the photon angles, $d^5\sigma/d\Omega_p d\Omega_\gamma dE_\gamma$ decreases smoothly with increasing photon energy up to $E_\gamma(\text{lab}) \simeq 80$ MeV. Above this photon energy the cross sections rise again. Our results are compared with the soft photon approximation and the external emission dominance calculations. The soft photon approximation describes most spectra fairly well up to $E_\gamma \simeq 100$ MeV and external emission dominance up to $E_\gamma \simeq 60$ MeV (lab), but both predict cross sections which are too small at the highest photon energies.

[NUCLEAR REACTIONS Proton-proton bremsstrahlung, $E = 730$ MeV; measured $\sigma(\theta, E_\gamma)$; compared with soft-photon calculations.]

I. INTRODUCTION

We report final results and the experimental details of the first investigation at medium energy of proton-proton bremsstrahlung ($pp\gamma$). The incident proton energy is well above the inelastic threshold in pp interactions and is substantially higher than the energies of all previous $pp\gamma$ experiments. An important objective of our experiment is to test the range of validity of the soft photon approximation (SPA) based on the Low[1] and Burnett-Kroll[2] theorems and that of the external emission dominance[3] (EED) approximation which is equivalent to the first term of the SPA expansion.

The Low theorem states that the first two terms in an expansion of the $pp\gamma$ amplitude in powers of the photon energy E_γ can be calculated using only information from the on-mass-shell process, i.e., the elastic pp phase shifts. The SPA is basically an evaluation of this Low amplitude. It is discussed in detail in Refs. 4–6, and specifics applying to this experiment are given in Sec. V. It follows from the Low and Burnett-Kroll theorems that the first term in the $pp\gamma$ cross section can be expressed as the elastic pp cross section times a known kinematic factor. This is the EED approximation, as discussed in Ref. 3 for the case of pion-proton bremsstrahlung ($\pi^\pm p\gamma$). A series of experiments on $\pi^\pm p\gamma$ in the vicinity of the $\Delta(1232)$ resonance[7-9] led to the surprising finding that the EED approximation is satisfactory for describing $\pi^\pm p\gamma$ up to the highest measured photon energy of 150 MeV. It is of interest then to see whether this same approximation applies as well to other hadron-hadron bremsstrahlung reactions such as $pp\gamma$.

Fresh interest in $pp\gamma$ and the applicability of EED at intermediate and high energy has been generated by the discovery of a large lepton-to-pion ratio[10] among the particles produced in high-energy hadron-hadron collisions. Calculations[11] in the standard Weizsäcker-Williams approach, using the EED approximation for the bremsstrahlung cross section, have provided some insight into the electromagnetic contribution to this lepton-to-pion ratio.

Many investigations of $pp\gamma$ in the past have focused on its possible use in determining off-mass-shell pp scattering amplitudes. An important objective thereby was to find a means of distinguishing between various models and potential recipes available for the nucleon-nucleon interaction. Previous $pp\gamma$ experiments[12] have been performed only at incident energies below 210 MeV, where the pp interaction is purely elastic scattering and a potential model description may be valid, and where mesonic effects such as those involving the $\Delta(1232)$ resonance are small. It appears that SPA is nearly sufficient to account for many of these measurements.[4,6] One might hope to find a substantial deviation from SPA by going to a new en-

ergy region where the pp interaction has a large inelastic component and where additional mechanisms may be important, as for example those involving an intermediate $\Delta(1232)$ resonance, $pp \rightarrow p\Delta^+ \rightarrow pp\gamma$. At $T_p = 730$ MeV (or $p_p = 1.38$ GeV/c), which is our choice of the incident proton energy, $\sigma_t(pp)$ is increasing rapidly with T_p and nearly half of $\sigma_t(pp)$ is due to inelastic channels. However, the energy is low enough so that phase shift solutions, albeit not very reliable ones, are available, thus making possible a full SPA calculation.

The principal complication introduced by our choice of incident momentum is the large π^0 production which forms a serious background. We have used an over-constrained detection setup to completely eliminate the π^0 background. Our experimental apparatus enabled us to measure the $pp\gamma$ differential cross section, $d^5\sigma/d\Omega_p d\Omega_\gamma dE_\gamma$, over a large range of photon energies, allowing a systematic study of the validity of SPA and EED as a function of the photon energy.

II. APPARATUS AND EXPERIMENTAL METHOD

A plan view of our apparatus is shown in Fig. 1. In describing the position of the detectors, we use an angular coordinate system (α, β) in which α is the angle of projection on the horizontal plane, measured clockwise from the beam direction, and β is the angle of elevation, measured upward from the horizontal plane. These angles are related to the conventional scattering angles θ (scattering angle measured from the beam line) and ϕ (azimuthal angle about the beam line) by the formulas $\cos\theta = \cos\alpha\cos\beta$ and $\tan\phi = -\tan\beta/\sin\alpha$.

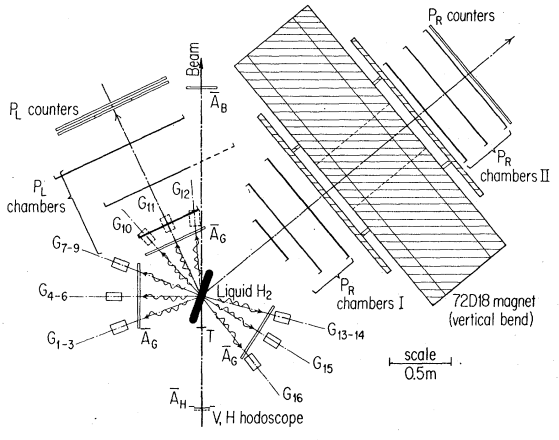

FIG. 1. Experimental apparatus. G_{1-16} are the photon counters, of which $G_{1,4,7,13,15,16}$ lie in the horizontal plane. The positions of the photon detectors are given in Table I and the proton detectors in Table II.

A. Beam and target

The experiment was performed in the external proton beam of the Lawrence Berkeley Laboratory 184 inch cyclotron. The beam was twice collimated, and steered by five bending magnets through a total deflection of 100° to produce a focal spot of 2.5 cm diameter on the hydrogen target. The average beam intensity was 10^6 protons per second. The momentum of the beam at the center of the hydrogen target was 1380 ± 10 MeV/c (kinetic energy 730 ± 8 MeV), as measured by range curves in copper and by wire-orbit measurements of the beam transport system. The momentum spread in the beam was less than 2%. The polarization of the beam is expected to be zero.[13]

The liquid hydrogen target consisted of a flask with two nearly flat, parallel walls of 0.13 mm thick Mylar, surrounded by a cylindrical gas ballast of 0.25 mm Mylar and 21 layers of 0.006 mm aluminized Mylar. This was mounted inside a cylindrical vacuum flask made of 0.8 mm aluminum. The width of the flask that contained the liquid hydrogen was 6.5 cm, including the slight bowing of the Mylar walls. The axis of the target was inclined at $20.5 \pm 0.5°$ to the beam line, giving an effective path length in liquid hydrogen of 18.6 cm.

B. Particle detectors

An incident proton was defined by the horizontal and vertical hodoscope planes (H and V in Fig. 1) and the timing counter T. The small beam halo was rejected by the veto counter $\bar{A}_H$ which surrounded the hodoscope.

Scattered protons were detected in a large magnetic spectrometer centered on an angle of 50.5° to the beam line, with its field horizontal so as to deflect particles downward. As the spectrometer was located to the right of the beam line (looking downstream), we shall refer to the proton detected in this arm of the experiment as P_R. The other final state proton, which must go to the left of the beam line, will be referred to as P_L. The trajectory of each P_R was measured by sets of three wire spark chambers before and after the magnet. A plane of four contiguous scintillation counters behind the magnet provided trigger information and allowed identification of portons by time-of-flight. The magnet gap was 46 cm wide by 183 cm high, and the counter plane had dimensions 64 cm × 183 cm. The horizontal angular acceptance of the spectrometer was

$$44° < \alpha_R < 57°.$$

The vertical angular acceptance depended somewhat on the momentum of the scattered particle. For 700 MeV/c protons it was

$-15° < \beta_R < 19°$;

the vertical asymmetry resulted from the downward deflection in the magnetic field. The typical solid angle acceptance was approximately 120 msr.

The second proton (P_L) was detected in a set of three spark chambers and two planes of scintillation counters in coincidence. This detector subtended the angles

$319° < \alpha_L < 351°$,

$-16° < \beta_L < 16°$,

and did not substantially limit the acceptance of $pp\gamma$ events except at the highest photon energies. Note that this detector restricts this experiment to accepting only the so-called first kinematical $pp\gamma$ configuration as discussed in Appendix A.

Photons were detected by 16 lead-glass Cherenkov counters (G_1–G_{16}), each 10 cm×10 cm in area and 15 cm (4.9 radiation lengths) thick. The construction and performance of these counters have been discussed elsewhere.[14] For on-axis photons the efficiency was (81±5)% at $E_\gamma = 20$ MeV and (92±2)% for $E_\gamma = 50$ MeV. Each group of photon counters was guarded by an anticoincidence counter ($\bar{A}_G$) to reject charged particles. Each photon counter subtended an angular range with respect to the center of the hydrogen target of approximately ±4.5° in each direction.

The position of the detectors is given in Tables I and II; this supersedes the values quoted in our earlier publication.[15]

TABLE I. Position of photon detectors. α is the horizontal projection of angle, measured clockwise from the beam line. β is the angle of elevation, measured upwards from the horizontal plane. R is the distance of center of face of photon counter to center of hydrogen target. $\theta_{c.m.}$ is the photon angle in center-of-mass system, measured from the beam line.

Photon counter G	α (deg)	β (deg)	R (cm)	$\theta_{c.m.}$ (deg)
1	250	−1	59	134
2	250	−19	59	137
3	250	−37	60	135
4	270	−2	59	122
5	269	−19	59	123
6	270	−37	59	122
7	292	−1	60	101
8	293	−19	59	102
9	292	−36	60	106
10	318	−38	69	86
11	335	−38	69	73
12	355	−39	69	66
13	104	1	56	133
14	105	−22	56	133
15	122	1	57	146
16	142	0	57	158

TABLE II. Position of proton detectors. Angles α and β are defined in the text.

Detector	α	β	Distance
P_R	44° to 57°	−15° to +19°	74 cm [a]
P_L	319° to 351°	−16° to +16°	157 cm [b]

[a] Center of hydrogen target to first P_R spark chamber.
[b] Center of hydrogen target to second plane of P_L counters.

C. Data acquisition

The coincidence logic required for an event trigger was

$$E = BGP_1P_2\bar{A}_G\bar{A}_B,$$

where G and P_1 represent logical "or" signals from the photon and spectrometer proton counters, P_2 is a coincidence between the two planes of counters of the P_L detector, $\bar{A}_G$ is the "or" of the photon anticounters, and $\bar{A}_B$ is a signal from the beam anticounter downstream from the target. B is the incident beam coincidence signal

$$B = V_i H_j T\bar{A}_H(\overline{V_m + H_m}),$$

where V_i and H_j are any counter in each of the beam hodoscope planes, T is the timing counter immediately before the target, $\bar{A}_H$ is the veto counter surrounding the hodoscope, and $(V_m + H_m)$ represents the triggering of two or more vertical or horizontal hodoscope counters and indicates multiple incident beam particles within our resolving time.

All information from the counters and spark chambers was processed by a Digital Equipment Corporation PDP-8/I computer. It stored the data on magnetic tape and provided on-line displays of various frequency distributions and the P_R and P_L trajectories in the chambers.

In addition to the runs taken with the standard "radiative" event trigger described above, we took several runs with the photon counters removed from the event trigger. These runs provided a measurement of the pp elastic scattering cross section, as well as a variety of systematic checks on the system. Runs with the target flask empty were taken in both triggering modes. After all analysis cuts were made, the background from the target walls amounted to less than 1% of the radiative or the elastic event rate.

III. ANALYSIS

A. Event reconstruction and data processing

The first part of the off-line analysis was the reconstruction of the trajectories of the two outgoing protons P_L and P_R of each event from the recorded spark chamber information. Events in which the P_L and P_R tracks did not project back to an intersection in the target volume were rejected. The momentum of P_R was calculated to an accuracy of 2% from the bend angle of the P_R track in the magnet. The momentum of the incident proton was well known (see Sec. IIA), and its direction was determined accurately using the position of the latched beam hodoscope counters and the intersection point of the P_L and P_R tracks. The direction of the outgoing photon was determined from the location of the photon counter which had fired.

The above measurements provide us with redundant information; each $pp \to pp\gamma$ event was overconstrained by two degrees of freedom. Consequently, we subjected every measured event to a two-constraint, least-squares fit to the hypothesis $pp \to pp\gamma$, making use of the measured values of the momentum vectors of P_R and the incident proton, and of the scattering angles of P_L and the photon. The fitting procedure minimized a χ^2-like variable constructed from the measured quantities, weighted according to their estimated errors. Each measured event can be characterized by this calculated pseudo-χ^2 value. The result of the data processing is illustrated in Fig. 2 where we have shown the pseudo-χ^2 distribution of all events that triggered photon counter G_7 and have a photon energy in the intervals 20–40 and 60–80 and 120–140 MeV. The peak in the spectrum at small χ^2 is due to $pp\gamma$ events, and the small, nearly flat remainder of the distribution is due to random background events and to $pp \to pp\pi^0$ events. The crosses and dots in this figure show the results of a Monte Carlo calculation of $pp\gamma$ and $pp\pi^0$ event distributions which will be discussed later.

The photon energy in this experiment was not measured directly but was calculated from the least-squares fit for each event, making use of the "best" values of the measured variables α_γ, β_γ, $\vec{p}(P_R)$, α_L, and β_L determined by the least-squares fit. The photon energy resolution was obtained from an analysis of Monte Carlo generated $pp\gamma$ events. Details of the Monte Carlo calculation are given in Appendix B. The resolution was found to depend on the photon energy and on the position of the photon counter. Table III lists the calculated standard deviation of the photon energy for photon counters $G_{7,11,12}$, the latter two located at the worst positions. In the limiting case of zero-energy photons, the photon energy resolution was determined by analyzing a sample of $pp \to pp$ elastic scattering events as $pp \to pp\gamma$ to obtain their fictitious "photon" energies. The results for $G_{1,12,13}$ are illustrated in Fig. 3. The standard deviations in the photon energy for all

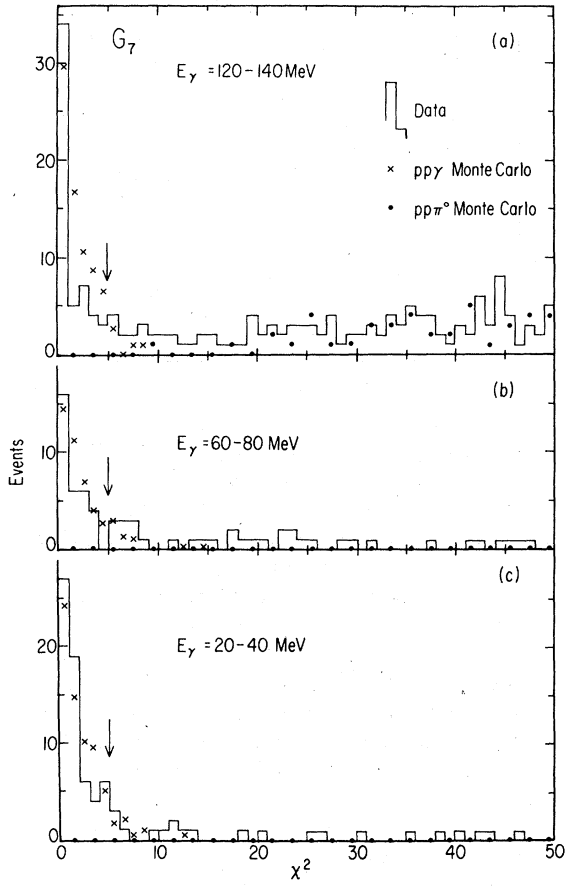

FIG. 2. χ^2 distribution of events recorded in photon counter G_7 for three photon energy intervals. The crosses indicate the distribution of a $pp\gamma$ sample and the dots a $pp\pi^0$ sample generated by Monte Carlo technique with reasonable values for the measurement errors. The $pp\gamma$ data sample used in the evaluation of the $pp\gamma$ cross section is defined as events with $\chi^2 < 5$ (indicated by the single arrow).

TABLE III. Photon energy resolution calculated by Monte Carlo technique for three photon counters and several photon energies. σ is the standard deviation.

		σ (MeV)					
	E_γ	25	50	75	100	125	150–200
Photon counter G					MeV		
7		4	4	5	6	7	
11		6	6	6	7	8	9
12		6	6	7	8	9	10

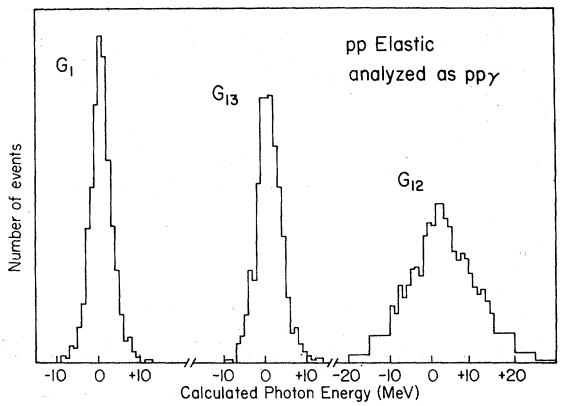

FIG. 3. Fitted "photon" energy of a sample of $pp \rightarrow pp$ elastic scattering events analyzed as $pp \rightarrow pp\gamma$ in the photon counters G_1, G_{12}, and G_{13}.

the counters are listed in Table IV; they fully support the calculated results given in Table III.

The estimated errors in the measured quantities, which are used as weight factors in the least-squares fit analysis of the measured event, have been carefully investigated. We made use of some special pp elastic scattering runs in which the large hydrogen target was replaced by a 6 mm strip of CH_2. The so-called "pull" quantities of the least-squares fit, which are the differences between the best fit and the central value of the measured quantities of each event divided by the estimated errors, were found to have a Gaussian distribution with a variance $\simeq 1$ for a sample of our data. This gives us confidence in the correct value of the errors used in the analysis.

B. Elimination of π^0 background

The principal difficulty in this experiment was the separation of $pp\gamma$ events from the unwanted background of π^0 production events ($pp \rightarrow pp\pi^0$) which triggered the apparatus. Fortunately, the kinematics of the two processes are sufficiently different that the possibility of a $pp\pi^0$ event masquerading as a $pp\gamma$ event can occur only in a very limited photon energy region which is near the high energy end of the photon spectrum. We can illustrate this point using the results of Monte Carlo simulations of the $pp\pi^0$ and $pp\gamma$ events which trigger our detectors. A brief account of the procedures followed in our Monte Carlo work is given in Appendix B.

The distinction between the $pp\gamma$ and $pp\pi^0$ events can be very clearly seen by considering the distributions of three kinematic variables measured in the experiment: θ_{RB} = angle between P_R and the incident proton direction, θ_{LB} = angle between P_L and the incident proton direction, p_R = momentum of P_R (measured in spectrometer). Figure 4 shows three contour plots in the kinematic variable space of p_R and θ_{RB} for photon counter G_7, obtained from a sample of Monte Carlo-generated $pp\gamma$ and $pp\pi^0$ events. The shaded area is the domain of all the $pp \rightarrow pp\pi^0$ events with both protons falling within the experimental acceptance of our detectors. The two dotted areas are the domains of two samples of $pp \rightarrow pp\gamma$ events with $E_\gamma = 60$ and 100 MeV, respectively. The Monte Carlo calculations included the uncertainties in all measured variables. It can be deduced from Fig. 5 that there is for each photon counter a certain photon energy, E_{clean}, below which there is no overlap between the $pp\pi^0$ and $pp\gamma$ domains. In other words, accepted events that have a photon energy smaller than E_{clean} are $pp\gamma$ events except for a few background events due to randoms in the photon counters and proton scattering in the target which were not considered in our Monte Carlo simulation of $pp\pi^0$ events. Such background events are eliminated with a χ^2 cut as described below. The different values of E_{clean} for the different photon counters are listed in Table V. The event sample with photon energies larger than E_{clean} may be contaminated by $pp\pi^0$ events. It is apparent from Fig. 4 that we can apply a simple cut to our data which removes all $pp\pi^0$ events without sacrificing many $pp\gamma$ events. This so-called π^0 cut removes events with kinematics below the dashed diagonal line and to the left of the dashed vertical line in Fig. 4. A similar acceptance criterion applies to the kinematic variable space of θ_{RB} and θ_{LB}. Specifically, the π^0 cut accepts events satisfying any one of the conditions:

$$\theta_{RB} > 51.5^\circ,$$

$$\theta_{RB} > 67^\circ - 0.035 p_R \ (\text{MeV}/c),$$

$$\theta_{RB} > 67^\circ - 0.889 \theta_{LB}.$$

The effect of the π^0 cut was included when we calculated the acceptance of our setup for $pp\gamma$. Only data with photon energy $> E_{\text{clean}}$ are affected.

It is of great interest to investigate the effect of the π^0 cut on the χ^2 distribution of our events. Figure 5 shows the number of events in G_6 versus their χ^2 value, in eight different photon energy intervals. When $E_\gamma < 80$ MeV [Figs. 5(a)–5(c)], the π^0 cut has no effect on the χ^2 distribution since it is not possible for a $pp\pi^0$ event to reconstruct as $pp\gamma$ with $E_\gamma < 80$ MeV. In the interval $80 < E_\gamma \leq 100$ MeV, the π^0 cut hardly affects the distribution at small χ^2, since the peak at $\chi^2 \sim 0$ is from $pp\gamma$ events, but removes most of the broad shoulder above $\chi^2 \sim 6$, reducing the shoulder to the level of the background in Fig. 5(c). The π^0 cut thus removes all $pp\pi^0$, leaving $pp\gamma$ unaffected as expected, since in this photon energy interval the $pp\gamma$ and $pp\pi^0$ re-

TABLE IV. List of experimentally determined photon counter resolutions for $E_\gamma = 0$ MeV, obtained by treating pp elastic as $pp\gamma$ events. σ is the standard deviation.

Photon counter G	σ (MeV)
1–6	3
7–9	4
10	5
11–12	6
13–16	3

gions do not overlap although they are very close. In the interval $100 < E_\gamma \leq 120$ MeV, the π^0 cut removes all $pp\pi^0$ but also removes some $pp\gamma$. The maximum possible photon energy for $pp\gamma$ with a photon in G_6 is 115 MeV. Many $pp\pi^0$ events, when analyzed as $pp\gamma$, have unphysical photon energies $E_\gamma > 115$ MeV. All such events are removed by our π^0 cut as illustrated in Figs. 5(f)–5(h). We define E_γ(max) as the maximum possible photon energy for a true $pp\gamma$ event in a given photon counter, taking into account the finite detector apertures and measurement errors; a list of E_γ(max) is included in Table V.

The effective discrimination of our analysis against $pp\pi^0$ is further illustrated in Figs. 6 and 7. The calculated photon energy in $G_{7,11}$ of a Monte Carlo generated sample of $pp\pi^0$ events, analyzed as if they were $pp\gamma$, is shown in Fig. 6. There are no events with $E_\gamma < 80$ MeV, consistent with the value for E_{clean} in Table V. The χ^2 distribution of Monte Carlo "$pp\pi^0$-as-$pp\gamma$" events in G_7 and G_{11}, without any restriction on the calculated photon energy, is shown in Fig. 7. This figure suggests that we can define a photon energy below which no $pp\pi^0$ can be analyzed as $pp\gamma$ with $\chi^2 < 20$. This is called E_{safe} and is listed for all photon counters in Table V.

The final phase of separating $pp\gamma$ events from the background is based on the χ^2 of the least-squares fit to every event. Our Monte Carlo simulation of $pp\gamma$ events, with careful consideration of the measurement errors, indicates that 93% of all $pp\gamma$ events have $\chi^2 < 5$ and that the χ^2 distribution closely matches the theoretical one for two degrees of freedom. In Fig. 2, we have compared

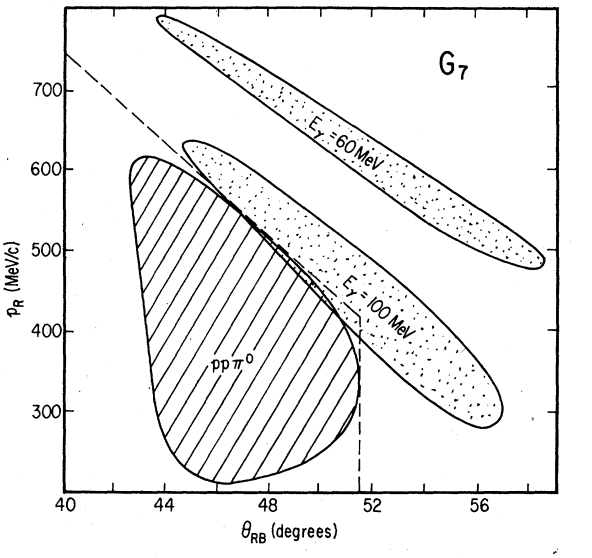

FIG. 4. Regions populated by $pp\pi^0$ events and $pp\gamma$ events in photon counter G_7, in the space of kinematic variables p_R and θ_{PR} defined in the text. The events were generated by a Monte Carlo simulation of $pp\gamma$ and $pp\pi^0$ events with reasonable measurement errors.

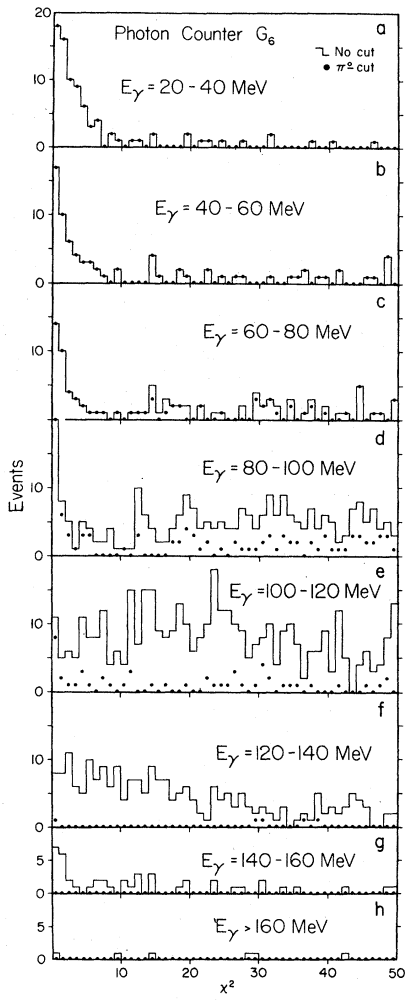

FIG. 5. χ^2 distribution of the events recorded in photon counter G_6 and analyzed as $pp\gamma$ candidates, grouped in 20 MeV wide bins in E_γ. Solid-line histogram: uncut data. Dots: after "π^0 cut" described in text has been applied.

TABLE V. List of "clean," "safe," and maximum photon energies for each photon counter as defined in the text. The finite detector apertures and measurement errors were considered in obtaining these numbers.

Photon counter G	E_{clean} (MeV)	E_{safe} (MeV)	E_γ (max) (MeV)
1	55	65	95
2	50	65	95
3	50	65	95
4	60	85	125
5	60	70	120
6	60	70	115
7	70	130	180
8	70	125	180
9	65	130	160
10	90	all	200
11	125	all	220
12	140	all	220
13	55	60	70
14	55	60	70
15	50	50	60
16	45	45	55

the χ^2 distributions of our data in G_7 with the Monte Carlo calculations. The $pp\gamma$ and $pp\pi^0$ Monte Carlo distributions agree very well with the experimental data. Not included in the Monte Carlo is a nearly uniformly flat background due to randoms in the photon counters and proton double scattering in the target.

C. Event selection

Besides the $pp\pi^0$ background discussed in the previous section, there was a small background in our experiment due to random coincidences between pp elastic scattering events and noise pulses from the photon counters. Such events satisfy the radiative scattering kinematics with $E_\gamma \simeq 0$ and give a small χ^2 value. The excellent photon energy resolution of our detection system allows us to eliminate such events by applying a photon energy cut, accepting all events with $E_\gamma > 15$ MeV. For events in photon counters $G_{7\text{-}12}$, which have a poorer energy resolution than the others (Table IV), we required $E_\gamma > 25$ or 35 MeV. The remaining random background was reduced by applying a cut of ±3 ns on the photon time-of-flight (TOF) and subsubtracting a small background based on the out-of-time event distribution. Some typical TOF distributions for different E_γ bins are shown in Fig. 8.

The number of $pp\gamma$ events for each counter and each photon energy interval was chosen to be the number of events with $\chi^2 < 5$ from our data sample obtained with the TOF and π^0 cuts. The numbers are listed in Table VI. Figures 2 and 5 indicate that there is about a 7% chance for good $pp\gamma$ events to have $\chi^2 > 5$, but the loss of good events by our $\chi^2 < 5$ cut is closely compensated by the intrusion of the flat χ^2 background under the low χ^2 peak. Two other background subtraction procedures yielded (within statistical errors) the same result as the simple cut at $\chi^2 < 5$.

D. Cross section calculation

The $pp \to pp\gamma$ differential cross section in the laboratory system for each photon counter G_i and each interval of photon energy E_γ is

$$\frac{d^5\sigma}{d\Omega_{PR}\, d\Omega_\gamma\, dE_\gamma} = \frac{\gamma}{BT\Delta E_\gamma (\Delta\Omega_{PR})_i (\Delta\Omega_\gamma \epsilon_\gamma)_i \epsilon_{sc} \epsilon_c \epsilon_{surv}}$$

where γ is the number of accepted events with reconstructed photon energy between $E_\gamma - \frac{1}{2}\Delta E_\gamma$ and

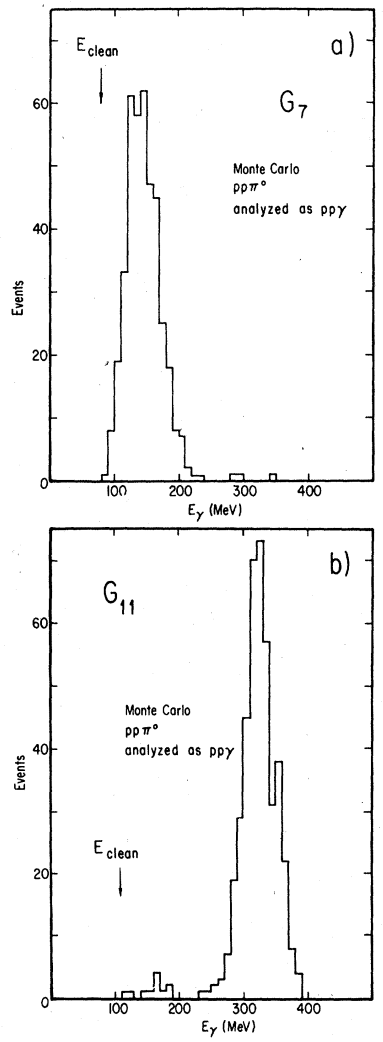

FIG. 6. Photon energy spectrum for Monte Carlo generated $pp\pi^0$ events analyzed as $pp\gamma$ in photon counters G_7 and G_{11}, without a cut on χ^2 or the π^0 cut.

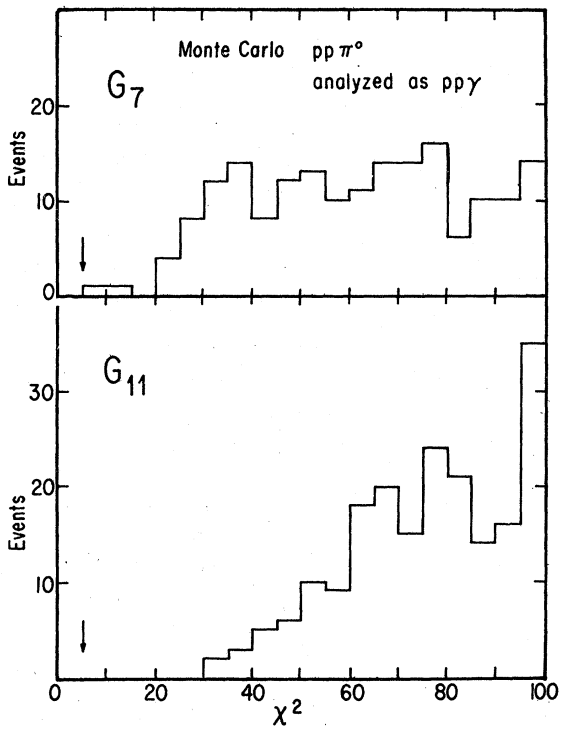

FIG. 7. χ^2 distribution for Monte Carlo generated $pp\pi^0$ events analyzed as $pp\gamma$ in photon counters G_7 and G_{11}, without a cut on photon energy or the π^0 cut. In the data analysis we make a cut at $\chi^2=5$, indicated by the vertical arrow.

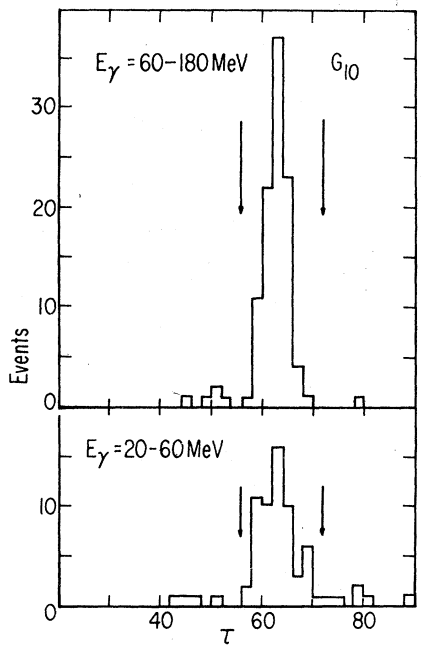

FIG. 8. Time-of-flight spectrum recorded in photon counter G_{10} for two photon energy bins. τ is the TOF channel number (one channel equals 0.38 ns). The vertical arrows define the in-time peak. Events outside the peak are due to randoms.

$E_\gamma \pm \frac{1}{2}\Delta E_\gamma$, B is the number of incident protons given by the number of beam coincidences B_C corrected for the attenuation of the beam in the target, event rejection due to randoms in anticounters, beam doubles and multiple photon counter latches, T is the number of protons per unit area traversed by the incident beam in the hydrogen target, ΔE_γ is the width of the photon energy interval, and $(\Delta\Omega_{PR})_i$ is the effective solid angle acceptance of our setup for protons from $pp\gamma$ with the photon in G_i. At low photon energies Ω_{PR} is equal to the solid angle acceptance of the P_R spectrometer, which is 120 msr. At high photon energies the $pp\gamma$ kinematics restrict the usable aperture of the magnet, and consequently Ω_{PR} is reduced and its effective central angle is shifted forward. The size and location of the P_L detector were such as to accept only the proton of $pp\gamma$ corresponding to $pp\gamma$ configuration number one, as defined in Appendix A. Because of kinematic correlations, Ω_{PR} depends on the direction and energy of the photon and was calculated separately for each photon counter by the Monte Carlo method. Results for $G_{10,12}$ are shown in Fig. 9. $(\Delta\Omega_\gamma)_i$ is the effective solid angle of photon counter i. It is obtained by a Monte Carlo calculation that includes the edge effects of the photon detectors and the effects associated with the extended size of our hydrogen target. ϵ_γ is the photon detection efficiency (see Sec. II D) determined in a separate experiment.[14] The accurate numerical values of ϵ_γ are useful only in conjunction with the value used for Ω_γ. For a typical photon counter (G_7), the product $\epsilon_\gamma\Omega_\gamma$ is 18.2 msr at $E_\gamma=17$ MeV, 21.8 at 25 MeV, and 24.3 at 160 MeV. ϵ_{sc} is spark chamber efficiency, calculated from comparisons of 2- and 3-spark fits in each set of spark chambers. ϵ_c is efficiency of the proton trigger counters. ϵ_{surv} is survival probability of outgoing particles, including proton interactions in P_L, proton and photon interactions in the target, vacuum chamber walls, air and spark chambers, and photon conversion in the photon anticounters.

Numerical values of these factors and corrections are given in Table VII.

IV. RESULTS

A. Differential cross sections for $pp \to pp\gamma$

The kinematics of each $pp\gamma$ event in the laboratory system is completely determined by the experiment, so we have the option of expressing the differential cross section in terms of any set of five independent variables. We have chosen $d^5\sigma/d\Omega_{PR}d\Omega_\gamma dE_\gamma$ (where $d\Omega_{PR}$ refers to the angles of proton P_R). The choice of dE_γ in this expres-

TABLE VI. Number of accepted $pp\gamma$ events for each photon counter and each interval of photon energy.

Photon counter	Energy interval (MeV)												
G	15–25	25–35	35–45	45–55	55–65	65–75	75–85	85–105	105–125	125–145	145–165	165–185	185–205
1	34	23	26	20	20	23	11						
2	38	31	20	14	14	14	9						
3	22	19	20	8	17	10	5						
4	37	36	33	17	13	21	22	27					
5	40	46	31	29	22	16	20	20					
6	35	27	21	24	16	16	20	29					
7		31	19	23	19	20	22	45	55	55			
8		34	33	29	14	21	22	36	52	48			
9		34	28	11	21	15	17	41	34	29			
10		11	8	12	11	6	10	22	24	36	30		
11			24	23	19	21	15	31	48	58	53	52	28
12			16	19	18	10	22	22	22	31	42	15	17
13		54	30	21	12	6							
14		41	38	24	19	10							
15		48	36	27	12								
16		40	25	19									

sion is a natural one, as the bremsstrahlung cross section for low energy photons varies as $1/E_\gamma$ according to the Low theorem. The other two differential elements $d\Omega_{PR}$ and $d\Omega_\gamma$ are chosen because the corresponding variables in the lab system are constant in our experiment except at high photon energy where the restriction in the detector apertures is apparent in Fig. 9.

We wish to call attention here to the fact that there are always two different kinematical configurations for $pp\gamma$ corresponding to the same set of lab variables defined by $d\Omega_{PR}d\Omega_\gamma dE_\gamma$. Fortunately, the kinematics of the two cases are sufficiently different that it is easy to distinguish between them by means of the other lab variables ($|\vec{p}_{PR}|$, θ_{PL}, ...) which do not appear explicitly in the phase space element. Our detector arrangement was, in general, sensitive to only one of the configurations, namely the one with the larger θ_{PL}, called configuration 1. All our cross section evaluations and comparisons with theory are based on the transformation between lab and center-of-mass variables of configuration 1. Details are given in Appendix A.

Our results for the differential cross sections in bins of photon energy in the lab system are given in Table VIII. The results presented here supersede previously reported preliminary results.[15,16] The dependence of $d^5\sigma$ on the photon energy for the individual photon counters is shown in Fig. 10. We have plotted $d^5\sigma/d\Omega_{PR}d\Omega_\gamma dE_\gamma$ in the laboratory system versus E_γ in the laboratory (lower scale). The upper scale gives the photon energy in the center-of-mass system. Some examples of the photon energy dependence of the differential cross section in the center-of-mass system for our preliminary results have been given in Ref. 16. The marked increase in $d^5\sigma$ (lab) at the high end of the photon spectrum results mainly from a rapidly increasing laboratory phase space factor (Appendix

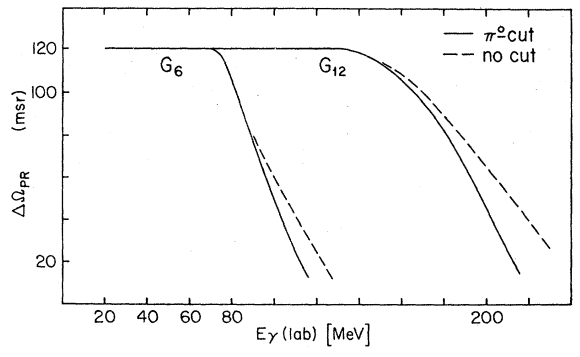

FIG. 9. Effective solid angle for detecting protons from $pp\gamma$, as defined in text, for two photon counters.

(a)

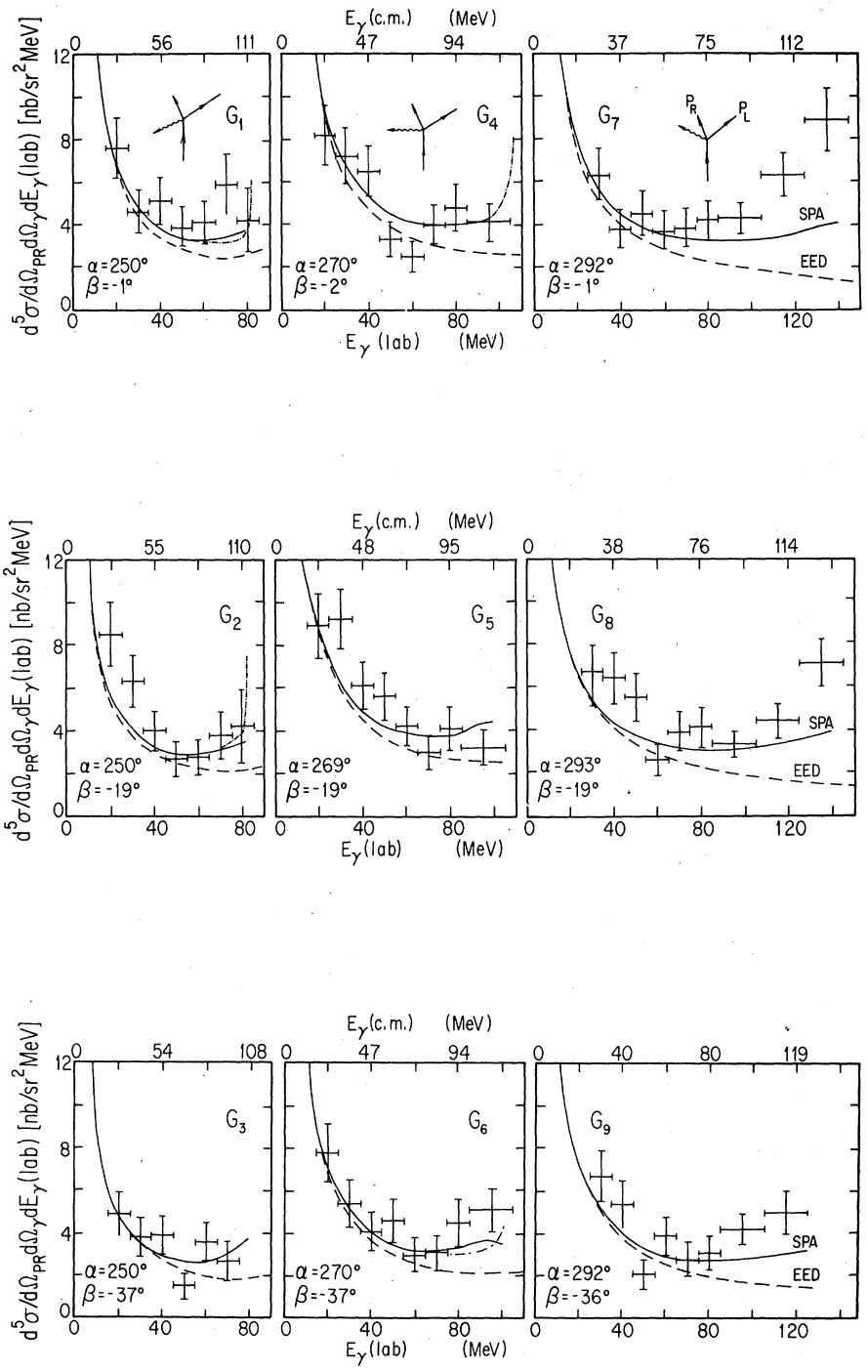

FIG. 10. Laboratory differential cross sections for all 16 photon counters as a function of the photon energy. The lower scale gives the photon energy in the lab and the upper scale in the center-of-mass. The solid curves are the SPA theoretical point cross sections multiplied by the factor S of Table IX, to average over the finite acceptance of the apparatus. The dashed curve is the EED calculation averaged by Monte Carlo method over the acceptance of the detectors. The dashed-dotted line, shown for a few counters, shows the SPA point calculation *not* averaged.

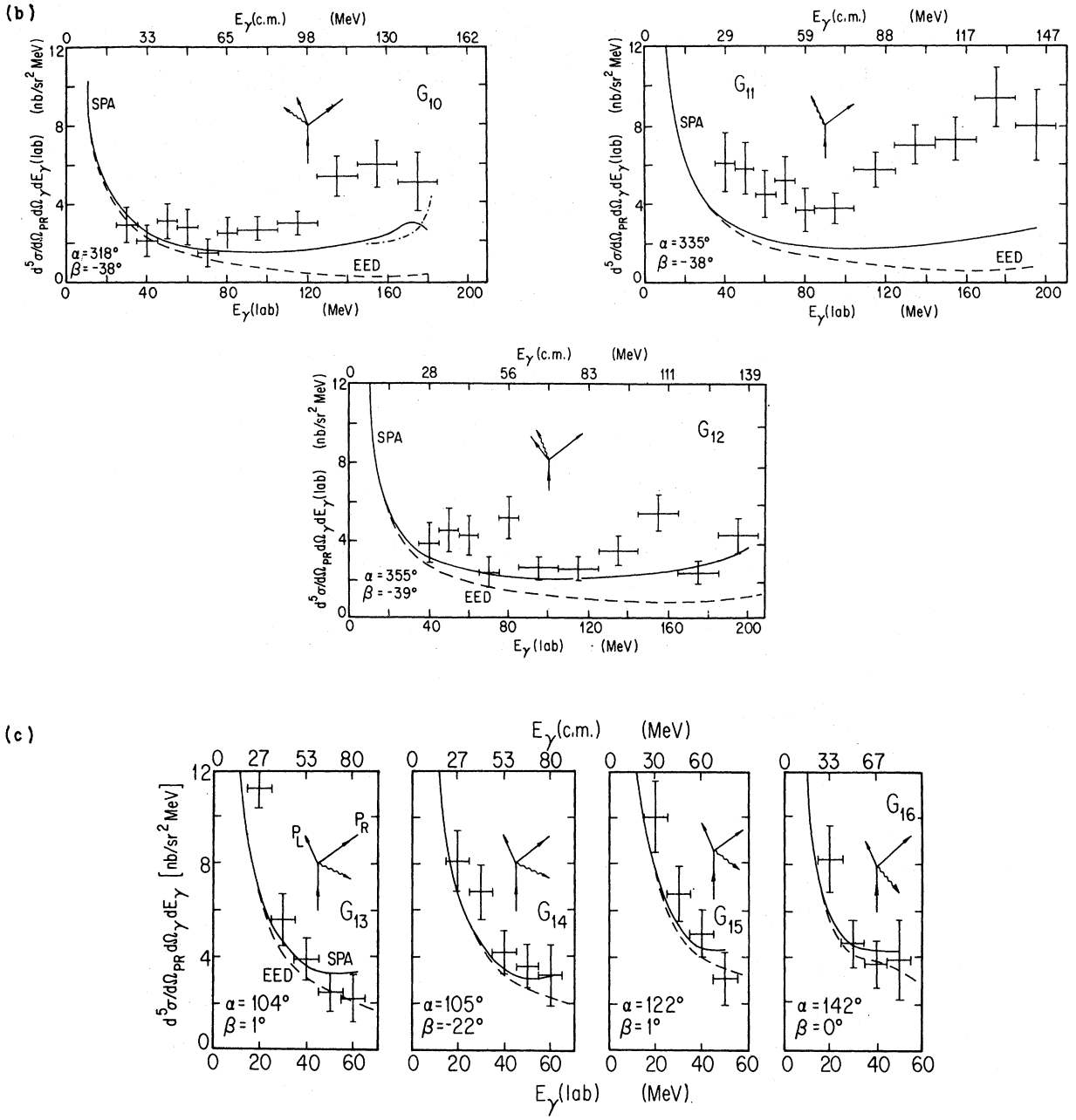

FIG. 10. (*Continued*).

A) and is not an indication of a rapidly increasing bremsstrahlung amplitude.

B. $pp \to pp$ elastic scattering result

We have also measured the differential cross section for pp elastic scattering, averaged over the acceptance of our spectrometer. This measurement provides a check on the acceptance and normalization of our experiment. The mean scattering angle for P_R is 51.5° in the laboratory, which corresponds to $\theta^*_{P_R} = 111°$ and $\theta^*_{P_L} = 69°$ in the c.m. system. The measured cross section in the c.m. is

$$d\sigma/d\Omega^* = 1.9 \pm 0.2 \text{ mb/sr}.$$

To compare this with previous measurements, we use the fits of Ryan *et al.*[17] to calculate the average cross section over our acceptance. The result

TABLE VII. Normalization factors and corrections used in cross section calculations.

$B_C = 3.48 \times 10^{11}$ protons
$T = (7.87 \pm 0.40) \times 10^{23}$ protons/cm^2
$\epsilon_{sc} = 0.845 \pm 0.015$
$\epsilon_c = 0.91 \pm 0.05$
Corrections
beam attenuation (3.1 ± 0.6)%
beam antincounter random rejection (6 ± 3)%
photon anticounter random rejection (2.5 ± 1.0)%
multiple photon counter (1.5 ± 0.2)%
multiple beam hodoscope counter (1.5 ± 0.2)%
P_L interaction loss (1.0 ± 0.2)%
P_R interaction loss (1.9 ± 0.4)%
photon interaction loss (2.3 ± 0.6)% to (3.5 ± 0.6)%

is

$$d\sigma/d\Omega^* = 1.9 \pm 0.2 \text{ mb/sr},$$

in agreement with our measurement.

C. Discussion of errors

A typical data point of our $pp\gamma$ experiment has some 50 events. Our results, therefore, have a statistical error of at least 15%.

There is also a systematic error not included in Table VIII or Sec. IV B, above, which we estimate to be 8%. It is due to the uncertainty in the target thickness, spark chamber efficiency, beam doubles, etc.

V. COMPARISON WITH THEORY

Traditionally $pp\gamma$ data have been compared with potential model calculations with the aim of unraveling off-shell aspects of the nucleon-nucleon

TABLE VIII. Laboratory differential cross sections $d^5\sigma/d\Omega_\gamma dE_\gamma$ in nb/sr^2 MeV for $pp \to pp\gamma$ at $T_p = 730$ MeV for different photon energy intervals. Errors are statistical only; not included is a normalization uncertainty of 8%.

Photon counter G	Photon energy interval (MeV) 15–25	25–35	35–45	45–55	55–65	65–75	75–85
1	7.6±1.4	4.6±1.0	5.1±1.1	3.9±0.9	5.1±1.0	5.9±1.4	4.2±1.5
2	8.5±1.5	6.3±1.2	4.0±0.9	2.7±0.8	2.8±0.8	3.8±1.1	4.2±1.7
3	4.9±1.0	3.8±0.9	3.9±0.9	1.5±0.6	3.6±0.9	2.7±0.9	2.3±1.1
4	8.2±1.4	7.2±1.3	6.5±1.2	3.3±0.8	2.5±0.7	4.0±0.9	4.8±1.1
5	8.9±1.5	9.2±1.4	6.1±1.1	5.6±1.1	4.2±0.9	3.0±0.8	4.1±1.0
6	7.8±1.4	5.4±1.1	4.1±0.9	4.6±1.0	3.0±0.8	3.1±0.8	4.5±1.1
7		6.3±1.2	3.8±0.9	4.5±1.0	3.7±0.9	3.8±0.9	4.2±0.9
8		6.7±1.2	6.4±1.2	5.5±1.1	2.6±0.7	3.9±0.9	4.1±0.9
9		6.7±1.2	5.4±1.1	2.1±0.7	3.9±0.9	2.8±0.8	3.1±0.8
10		2.9±0.9	2.1±0.8	3.1±0.9	2.8±0.9	1.5±0.7	2.5±0.8
11			6.1±1.4	5.8±1.3	4.5±1.2	5.2±1.2	3.7±1.1
12			3.8±1.0	4.5±1.1	4.2±1.0	2.3±0.8	5.1±1.1
13	11.2±1.7	5.6±1.1	3.9±0.9	2.5±0.8	2.2±1.0		
14	8.1±1.3	6.8±1.2	4.2±0.9	3.6±0.9	3.2±1.3		
15	10.0±1.5	6.7±1.2	5.0±1.0	3.1±1.1			
16	8.2±1.4	4.6±1.0	3.7±1.0				

Photon counter G	85–105	105–125	125–145	145–165	165–185	185–205
4	4.1±0.8					
5	3.2±0.8					
6	5.1±1.0					
7	4.3±0.7	6.3±1.0	8.9±1.5			
8	3.3±0.6	5.4±0.8	7.1±1.1			
9	4.2±0.7	5.0±1.0	7.1±1.6			
10	2.7±0.6	3.0±0.6	5.4±1.0	6.0±1.2		
11	3.7±0.7	5.7±0.9	7.0±1.0	7.3±1.1	9.4±1.5	8.0±1.8
12	2.5±0.6	2.5±0.6	3.5±0.7	5.4±0.9	2.3±0.6	4.2±1.2

potential.[18] Such an approach is not useful here since the initial energy is sufficiently high that relativistic and inelastic effects are important and potential models are not applicable. Alternatively, one can compare with soft photon calculations to see how much of the data can be explained by purely on-shell information obtainable from elastic scattering. This approach is of particular interest since in π-p bremsstrahlung, for reasons not yet completely understood, soft photon approximations describe essentially all of the data,[7-9] even in the region of the $\Delta(1232)$ resonance.

A. Soft photon approximation

A detailed SPA calculation of $pp\gamma$ has been performed by one of the authors and is discussed in Ref. 6. Here we simply review the basic features and quote some results of the calculation appropriate to this experiment.

The soft photon theorem, originally derived by Low[1] and put in a form appropriate for $pp\gamma$ by others,[4-6] states that if the amplitude for $pp\gamma$ is expanded in powers of the photon momentum k (note: in this section, we use k for the photon momentum) as follows:

$$M_{pp\gamma}=\frac{A}{k}+B+Ck+\cdots , \tag{5.1}$$

then gauge invariance determines the leading two terms A and B in terms of known kinematic functions and the on-shell elastic scattering amplitudes. The first term is particularly simple, as A is proportional to the full pp elastic amplitude. (B depends on the derivatives of the amplitudes as well.) The C and higher terms contain a combination of off-shell information, higher order on-shell terms, etc., and are unknown except in the context of a particular model.

The $pp\gamma$ cross section can be written schematically as

$$d\sigma(pp\to pp\gamma)\sim k|M_{pp\gamma}|^2 = \frac{A^2}{k}+2\,\mathrm{Re}AB^*+(B^2+2\,\mathrm{Re}AC^*)k+\cdots . \tag{5.2}$$

The factor k multiplying $|M_{pp\gamma}|^2$ originates in the phase space factor, discussed below. Again, the leading two terms, and now also the B^2k part of the third term, are given by the soft-photon theorem in terms of elastic scattering amplitudes.

There is some freedom in the choice of the kinematic point at which to evaluate the elastic amplitudes. However, it can be shown[2,19,20] that different choices affect the result only in order k, i.e., only in the third term containing the unknown C.

For the results discussed below, the generalized Low prescription[4] was used, i.e., the elastic amplitude was evaluated at average values of energy and momentum transfer given by

$$\bar{s}=\tfrac{1}{2}(P_1+P_2)^2+\tfrac{1}{2}(P_3+P_4)^2$$

and (5.3)

$$\bar{t}=\tfrac{1}{2}(P_1-P_3)^2+\tfrac{1}{2}(P_2-P_4)^2 ,$$

where the P_i's are the four-momenta of the four protons. Specifically, P_1 refers to the incident proton, P_2 to the target proton, P_3 to P_R, and P_4 to P_L; thus $P_1+P_2=P_3+P_4+k$.

Following these preliminaries, it is interesting to look at some numerical results. For the SPA calculations of Ref. 6, the individual amplitudes A/k and B were constructed explicitly, according to Eq. (2.4) of Ref. 5, using elastic pp amplitudes which were themselves constructed from elastic phase shifts. The resulting amplitude $(A/k)+B$ was squared and hence the cross section contains the leading two terms of Eq. (5.2) and the B^2k part of the third term. The elastic phase shifts were taken from MacGregor, Arndt, and Wright[21] with the modification in the imaginary $^1D_2$ phase suggested by Willard *et al.*[22] This phase shift solution does not include as input the new cross section data in the relevant 500–750 MeV range and so must be considered approximate. It does, however, reproduce the data of Ref. 22 to better than 15–20%, which can be taken as a rough upper limit on the uncertainty in the results for the first two terms due to ambiguities in the elastic scattering information. The calculation of the B^2k term requires the elastic amplitudes rather than the cross sections. Therefore, it may be more sensitive to uncertainties in the phase shifts than the first two terms. For this reason, in the high k region where the B^2k term is important, the SPA results could possibly be uncertain by significantly more than 20%.

It is of interest to compare the individual terms A^2/k^2, $2\,\mathrm{Re}AB^*/k$, and B^2 in the square of the invariant amplitude of SPA, $|M_{pp\gamma}|^2$, which are plotted for some typical counters in Figs. 11(a) and 11(b). (Note that A and B are *not* constants, but kinematic expressions of zeroth order in k.) For all values k relevant here, the $2\,\mathrm{Re}AB^*/k$ term is much less than the A^2/k^2 term. Furthermore, for $k\lesssim 100$ MeV, the A^2/k^2 term is greater than the B^2 term. These two observations mean that for $k\lesssim 100$ MeV, the leading two terms of the SPA, and particularly the first term alone, should dominate the cross section. Above $k\sim 100$ MeV, the B^2 term be-

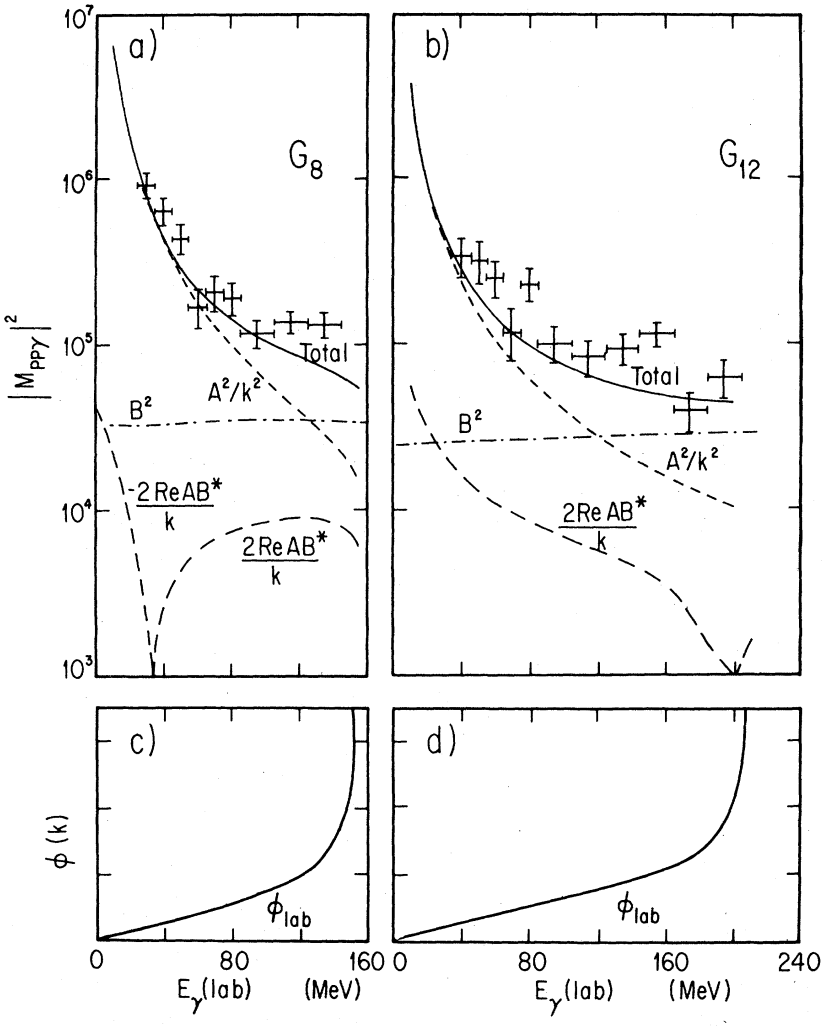

FIG. 11. (a), (b) The square of the SPA invariant amplitude and its individual terms A^2/k^2, $2\,\mathrm{Re}AB^*/k$, and B^2, as a function of the photon energy for photon counters G_8 and G_{12}. The crosses are our data points divided by the phase space factor and the acceptance factor S defined in the text. (c), (d) Phase space factor $\phi(k)$ (arbitrary units) versus photon energy in the lab system.

comes the dominant one. Since the B^2 term varies only slightly with photon energy, the k dependence of the cross section in this region is approximately proportional to the phase space factor $\phi(k)$ which is shown in Figs. 11(c) and 11(d). In the laboratory $\phi(k)$ is nearly proportional to k for small k and it rises to a singularity at $k_{\max}$.

In Fig. 10 we have plotted along with the data the SPA calculation averaged over the counter acceptance by multiplying it by the correction factor S as discussed in Sec. V D. In a few cases we show also the point (unaveraged) SPA result to indicate the effect of the averaging on the theoretical prediction.

As can be seen from Fig. 10, for small k the data are generally well fit by the SPA calculation which is dominated in this region by the leading A^2/k term (essentially identical to the curve labeled EED, discussed below). At larger k, the leading term is not sufficient and the inclusion of the higher order terms in SPA leads to a considerable improvement in the fit to the data, though the calculations still fall significantly below the data at the highest photon energy. Note that the increase in the SPA cross section at larger k is essentially due to phase space, since the B^2 piece of $|M_{pp\gamma}|^2$ which dominates in this region is nearly constant. The only counter that shows a real conflict at low E_γ between SPA and our data is G_{11}. The experimental data are systematically higher than the theory, though the shape of the data appears consistent with other counters. We do not have a satisfactory explanation for the discrepancy.

The fact that the data in almost all counters agree, within errors, with the soft photon calculation both in normalization and shape in the small k region is encouraging as it gives us confidence in the essential correctness of the data. The discrepancies at large k are also interesting, indicating possible non-SPA effects.

B. External emission dominance

Burnett and Kroll[2] have shown that the first two terms of the bremsstrahlung *cross section* can be written as an operator acting on the elastic *cross section*. The first term of the soft-photon bremsstrahlung cross section, which dominates at low photon energy, can be written in a particularly simple form as a kinematic factor multiplying the elastic cross section:

$$\frac{d\sigma^{\text{lab}}}{d\Omega_3 d\Omega_k dk} = \frac{-\alpha}{4\pi^2 m P_1} \frac{kP_3^{\,3}}{|P_3^{\,2}E_4 - E_3 \vec{P}_3 \cdot \vec{P}_4|} \left[\frac{P_1^\mu}{k\cdot P_1} + \frac{P_2^\mu}{k\cdot P_2} - \frac{P_3^\mu}{k\cdot P_3} - \frac{P_4^\mu}{k\cdot P_4}\right]^2 \left[\bar{s}\,\frac{d\sigma_{pp}^{\text{c.m.}}}{d\Omega^*}(\bar{s},\bar{t})\right]. \tag{5.4}$$

It was found by two of the authors[3] that the corresponding expression for πp bremsstrahlung works extremely well in describing the experimental data for that reaction. The approximation Eq. (5.4) has, perhaps with some semantic imprecision, been labeled "external emission dominance" (EED). Curves representing the EED calculation for this experiment, averaged over the experimental acceptance by Monte Carlo calculations, are shown with the data and SPA calculations in Fig. 10.

Since expression (5.4) is equivalent, in concept, to the leading term of the SPA, the two curves should approach each other as $k \to 0$, as they do. Residual differences between EED and SPA at small k come from two sources. First, calculating the elastic *cross section* at average $\bar{s}$ and $\bar{t}$ according to Eq. (5.4) is slightly different from evaluating the *invariant amplitudes* for elastic scattering at $\bar{s}$ and $\bar{t}$ with the wave functions at appropriate radiative variables as is done in the SPA evaluation of Eq. (5.2). Numerically, the difference in our case is very small, see for example Fig. 3 of Ref. 6. Second, in the EED calculation we used the Ryan[17] parametrization of the elastic cross section instead of constructing it from phase shifts as was done for SPA. This leads to a slightly different elastic cross section, which enters as an overall factor in the leading term. After accounting for these differences, the difference remaining at larger k comes from the extra terms, in particular the B^2 term, which are included in the SPA calculation. (The EED calculations plotted in Ref. 15 differ slightly from the present values because of a computation error which has been corrected.)

Although the full SPA calculation agrees with the data up to substantially higher photon energies than does EED, the latter has several useful features which merit its presentation in this paper. The direct proportionality of the EED result to the elastic cross section makes the assignment of errors to the calculation very transparent. In addition, the simplicity of Eq. (5.4) makes the evaluation of the EED cross section by computer extremely fast and inexpensive, a considerable benefit when Monte Carlo calculations are used to evaluate the effects of experimental acceptance.

C. Model calculations

The discrepancy between the data and SPA calculations above 100 MeV may indicate possible non-SPA effects. It is of interest to speculate on the origins of the deviation. It must involve a contribution from the Ck term of Eq. (5.1), giving rise to the terms $(2\,\mathrm{Re}AC^*)k$, $(2\,\mathrm{Re}BC^*)k^2$, C^2k^3 in the cross section, any of which may predominate, depending on the relative sizes and phases of A/k, B, and Ck. A possible physical mechanism which produces a contribution to the Ck term is the Δ radiative decay diagram [Fig. 12(a)] which has been considered by Szyjewicz and Kamal,[24] and by Tiator, Drechsel, and Weber.[25] In the calculation of Szyjewicz and Kamal, the Δ contribution is calculated in a field theory model, without form factors, and added to the contributions from one boson exchange[24] (OBE) [Fig. 12(b)]. These OBE terms are obtained using parameters fitted to elastic data below 350 MeV. At 750 MeV they do not reproduce either elastic scattering or bremsstrahlung data in the soft photon region very well. Consequently, it was necessary to divide the OBE contribution to the $pp\gamma$ cross section by a factor of 16 to normalize to the small k region. The results obtained for the coherent addition of the two contributions do reproduce the data rather well. In-

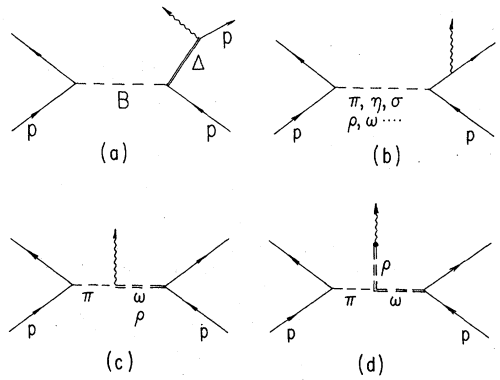

FIG. 12. Graphs for photon-proton bremsstrahlung. (a) Δ excitation contribution; (b) one boson exchange, external emission; (c) ω or ρ radiative decay contribution; (d) vector meson contribution.

terference effects are of the order of 20%. However, it should be noted that the OBE contribution normalized to $k=0$ looks at large k something like the leading term of the SPA, and in particular falls significantly below the full SPA calculation.[6] If the full SPA calculation were used instead, the results would be somewhat higher, tending to fall above the data.

In the calculation of Tiator *et al.*,[25] the Δ graph is calculated in a similar fashion, except that form factors are used, which reduce the Δ contribution by factors of 1.5–2.5 when both π and ρ exchange diagrams are included in Fig. 12(a), and by factors of 5–10 when only π exchange is considered. The result is added incoherently to the leading term of the SPA. Thus the interference terms are not included. Again, since the dominant B^2 part of SPA is not included at large k, the total results in this region may be significantly too small. Nevertheless, a quite reasonable fit to the data is obtained. Thus it appears that the Δ diagram is at least a candidate for explaining the deviation from SPA at large k.

However, there are other possibilities. We tried, for example, a phenomenological amplitude Ck, which we took as a constant times $(P_1^\mu k\cdot P_2 - P_2^\mu k\cdot P_1)$. This is the simplest form we could think of which is of order k, gauge invariant, and constant in the sense that it does not depend on any final kinematics but only on the initial energy. Using this amplitude, with the full SPA, an appropriate choice of the constant could be made so as to obtain a fit to the data just as good as those involving the Δ diagram. Furthermore, this term, with the same constant, produced a very small change in the results at 200 MeV,[6,12] well within experimental uncertainties.

The conclusion one draws, therefore, is that the important content of the difference between data and SPA at large k is not the distinctive resonance behavior of the Δ diagram but a single constant corresponding to the normalization of the Ck amplitude. Thus, as long as there are uncertainties in form factors, coupling constants, and background amplitudes in the Δ diagram, all of which affect the normalization, we cannot be certain that it is the important contributor. Experiments at higher energies above the resonance could be conclusive, since they would make it possible to trace out the distinctive resonance behavior of the Δ amplitude, whereas a simple constant amplitude such as the one we tried would increase monotonically with increasing energy.

Another possible physical mechanism suggested for producing a deviation from SPA behavior involves the direct participation of vector mesons in the photon emission process. Szyjewicz and Kamal[26] have calculated the ω contribution to $pp\gamma$, as illustrated in Fig. 12(c), in a Lagrangian model. Since experimentally $\Gamma(\omega\to\pi\gamma)\simeq 25\,\Gamma(\rho\to\pi\gamma)$, this contribution presumably dominates the radiative decay contribution of the vector mesons. They find that the ω contribution increases from 0.3% at $T_p=158$ MeV to 7% at $T_p=400$ MeV. The contribution at our incident energy has not yet been evaluated.

Figure 12(d) shows an example of the type of process that has been evaluated by Rückl[27] in a vector-meson-dominance calculation of $pp\gamma$ which should be most applicable at high E_γ. He obtains a contribution to the $pp\gamma$ cross section which is proportional to k and provides a reasonable description of our data for $E_\gamma>100$ MeV.

D. Effect of apparatus acceptance

To compare theoretical predictions with data, it is necessary to take into account the finite size of our detectors, described in Sec. II B. We recall that a photon counter subtends approximately ±4.5° horizontally and vertically. The P_R detectors subtend ±7° horizontally and ±17° vertically with the vertical acceptance centered at $\beta=2°$. The P_L detector is sufficiently large not to affect the acceptance save for the highest energy photons. We have used the Monte Carlo technique to average the theoretical cross section over the aperture of our counters. This results in a correction factor S which must be multiplied into the appropriate theoretical point geometry cross section to obtain an averaged theoretical cross section for comparison with the data. The correction factor S is defined

$$S=\frac{d\sigma(pp\gamma,\ \text{SPA Monte Carlo averaged})}{d\sigma(pp\gamma,\ \text{SPA point calculation})}\,. \tag{5.5}$$

It varies somewhat for different photon counters and energy bins, usually between 0.9 and 1.1, and is listed for some photon energies in Table IX. To calculate S we used a simplified SPA in which $|M_{pp\gamma}|^2$ consisted of the EED expression plus a constant term which is set equal to the A^2/k^2 term at the same photon energy where, in the full SPA, the A^2/k^2 term is equal to the B^2 term. The theoretical point cross section is calculated for a monochromatic incident pencil proton beam of $T_p=730$ MeV with the P_R scattered at $\alpha=50.5°$ and $\beta=+2°$ and the photons going to the center of the photon counters.

The effect of the averaging over the acceptance is most apparent for high energy photons. The theoretical point cross section increases sharply when k approaches $k_{\max}$ as a consequence of a

TABLE IX. Modification of point cross sections (at $\alpha_{PR}=50.5°$ and $\beta_{PR}=2°$) to take into account the finite aperture of the detectors. Listed are the calculated values of the ratio S for different photon counters, as described in text, and

$$S=\frac{d^5\sigma(pp\gamma, \text{SPA, Monte Carlo averged calculation})}{d^5\sigma(pp\gamma, \text{SPA, point calculation})}.$$

Photon counter G	E_γ(lab) (MeV) 40	60	80	100	120	140	160	180	200
1	0.94	1.00	1.05						
2	0.96	1.02	0.85						
3	0.97	1.06	1.09						
4	0.91	0.93	1.01	0.93					
5	0.94	0.95	1.02	0.89					
6	0.97	0.98	1.10	0.83					
7	0.98	0.97	0.97	1.02	0.99	0.98			
8	0.94	0.94	0.94	0.97	1.06	0.99			
9	0.96	0.94	1.02	1.07	1.05				
10	0.96	0.98	1.00	1.00	1.06	1.10	1.14	0.73	
11	1.02	1.01	1.00	1.01	1.00	1.06	1.13	1.18	0.96
12	1.13	1.13	1.10	1.05	1.06	1.08	1.14	1.14	1.01
13	0.99	1.23							
14	0.94	1.11							
15	0.97								
16	1.06								

singularity in the phase space factor. The "averaged" cross section, on the other hand, may decrease, making the theoretical predictions near k_{max}, shown in Fig. 10, look rather peculiar at times.

VI. CONCLUSIONS

Our measurements of the differential cross section for proton-proton bremsstrahlung at an incident energy of 730 MeV at 16 photon angles agree with the best available soft-photon approximation calculation up to a photon energy of approximately 100 MeV, and its leading term alone describes the data up to about 60 MeV. Thus neither the presence of the strong Δ resonance in the intermediate state nor the high degree of inelasticity in the pp elastic scattering amplitude appears to affect the applicability of the Low theorem up to $E_\gamma \sim 100$ MeV. For larger photon energies, the data lie substantially above the soft-photon calculations, rising with E_γ in the lab system. A possible explanation of this departure from the SPA calculation is a sizable contribution from the radiative deexcitation of the Δ isobar in the intermediate state $pp \to p\Delta^+ \to pp\gamma$, though any mechanism leading to a sufficiently large contribution of order k to the $pp\gamma$ amplitude will do as well.

ACKNOWLEDGMENTS

This research is supported by the U. S. Department of Energy (B.M.K.N., O.R.S., D.I.S.) and by the National Research Council of Canada (H.W.F.). We thank the Lawrence Berkeley Laboratory for the hospitality extended to us and the personnel of the LBL 184 in. Cyclotron for their dedicated help. Bill Plumlee and Nancy Matz were very helpful with the data taking. The data analysis was much helped by the efforts of Mike O'Neill and Grant Webster. One of us (H.W.F.) would like to thank Dr. J. G. Rogers for helpful discussions of the experimental technique and data analysis. The others wish to thank Dr. R. Rückl for useful theoretical discussions.

APPENDIX A: KINEMATICS AND TRANSFORMATIONS

A minor complication associated with calculating the cross section in the laboratory system is that the element of three-body phase space $d\Omega_{PR}d\Omega_\gamma dE_\gamma$ is double-valued, corresponding to two distinct kinematic configurations in the center-of-mass. Configuration one approaches the elastic scattering kinematics as $E_\gamma \to 0$. Configuration two, with the same values of the photon energy, photon angle and P_R angle in the laboratory, is characterized by a very small P_R energy and a very forward P_L angle in the laboratory. Figure 13 shows a vector diagram of the momenta of the outgoing particles in coplanar $pp\gamma$ geometry with a 120 MeV (lab) photon directed toward counter G_7. Configurations one and two have identical values of the photon angle, photon momentum, and P_R angle in the laboratory but different values of the P_R and P_L momentum

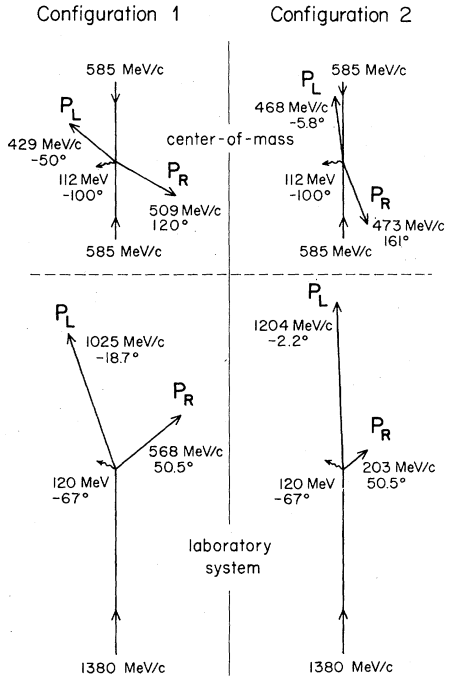

FIG. 13. Vector diagram of final state momenta in a coplanar $pp\gamma$ event with $E_\gamma = 120$ MeV (lab) in counter G_7. The double-valuedness of the three-body phase space $d\Omega_{PR} d\Omega_\gamma dE_\gamma$ results in two configurations which have identical α_γ, β_γ, α_{PR}, and β_{PR} in the lab. Configuration 2 is generally undetectable with our setup.

and the P_L angle. Configuration two is almost never detected in our experiment because the very forward P_L angle makes the proton miss our left proton detector and furthermore the P_R energy is too low for detection. The two configurations coalesce when the photon energy is at the maximum kinematically allowed value for the specified angles. Only when the photon energy is within about 10 MeV of this kinematic limit is there any possibility of detecting an event corresponding to the second configuration. We do not quote a cross section in this E_γ region, since it is also characterized by a small and rapidly varying acceptance.

To convert the laboratory cross sections $d\sigma/d\Omega_{PR} d\Omega_\gamma dE_\gamma$ given in Sec. IV to center-of-mass cross section $d\sigma/d\Omega^*_{PR} d\Omega^*_\gamma dE^*_\gamma$, we use the factor J which is given by

$$\frac{d^5\sigma}{d\Omega_{PR} d\Omega_\gamma dE_\gamma} = J \frac{d^5\sigma}{d\Omega^*_{PR} d\Omega^*_\gamma dE^*_\gamma}, \tag{A1}$$

where

$$J = \frac{d\Omega^*_{PR} d\Omega^*_\gamma dE^*_\gamma}{d\Omega_{PR} d\Omega_\gamma dE_\gamma} = \frac{E_\gamma p_{PR}{}^3}{E^*_\gamma p^*_{PR}{}^3} \frac{p^*_{PR}{}^2 E^*_{PL} - E_{PR} \vec{p}_{PR} \cdot \vec{p}^*_{PL}}{p_{PR}{}^2 E_{PL} - E_{PR} \vec{p}_{PR} \cdot \vec{p}_{PL}}. \tag{A2}$$

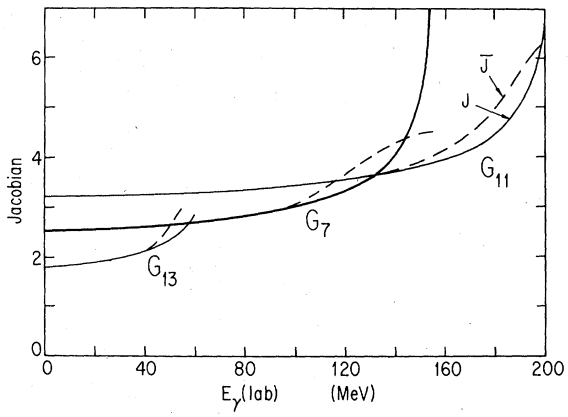

FIG. 14. Solid curves: Jacobian factor J (= ratio of lab to center-of-mass cross section) for three photon counters, calculated in point geometry. Dashed curve: $\bar{J}$ = Jacobian factor averaged over the detector acceptance.

The Jacobian for $G_{7,11,13}$ for configuration one is shown in Fig. 14. Note the sharp increase near the highest allowed E_γ, which is due to the singularity in the laboratory phase space already seen in Figs. 11(c) and 11(d). Averaging over the acceptance of our detectors always eliminates the singularity, as is seen in the curves labeled $\bar{J}$ in Fig. 14.

We do not quote here any of our cross sections in the center-of-mass system because the acceptance of our detectors in c.m. variables is not constant, making the interpretation of the results more complicated.

APPENDIX B: MONTE CARLO SIMULATION OF $pp\gamma$ AND $pp\pi^0$ EVENTS

The presence of the large background of $pp\pi^0$ events (which we estimate as $1/\alpha$ times larger than the $pp\gamma$ rate) made it imperative to investigate to what extent $pp\pi^0$ events could simulate $pp\gamma$ events. Since our photon detectors measured the angle of the photon but not its energy, it was in principle possible for a $pp\pi^0$ event with one photon detected to exactly duplicate the measured variables of a high-E_γ $pp\gamma$ event, although the phase space for such an exact coincidence is vanishingly small. Because of the lack of three-body coplanarity in the final state, nearly all $pp\pi^0$ events would yield a rather poor fit to the $pp\gamma$ reaction. In order to determine quantitatively the possibility of misidentifying a $pp\pi^0$ event as a $pp\gamma$ event, we made extensive Monte Carlo calculations in which both types of event were generated, randomly perturbed with estimated measurement errors, and

reconstructed using the same least-squares fitting procedure that was applied to the experimental data.

The procedure for the generation of the two classes of events varied slightly. In both cases, the direction and momentum of the incident particle and the point of interaction in the target were generated according to the experimental distributions. For $pp\gamma$ events, the program generated photons of fixed energy distributed uniformly over the face of each photon counter and then distributed one outgoing proton uniformly across the aperture of the magnetic spectrometer. The remaining variables were calculated from energy and momentum conservation. For $pp\pi^0$ events, the direction of the π^0 was generated isotropically in the center-of-mass system. The center-of-mass momentum p^* of the π^0 was generated with a spectrum proportional to p^*. Both of these assumptions are consistent with the experimental data of Cence *et al.*[23] The P_R proton direction was thrown as for the $pp\gamma$ events.

Since the laboratory momenta of the produced π^0's are on the average fairly small, so that the decay γ's are not strongly correlated with π^0 direction, we assumed no correlation between the π^0 direction and the position of the triggered photon counter. In order to provide a realistic approximation to the measured events, the kinematic variables were perturbed with normally-distributed measurement errors whose variances were obtained from the fitting of experimental events. When the resulting Monte Carlo $pp\gamma$ events were analyzed using the least-squares fitting program, the resulting χ^2 distribution (Fig. 2) was in excellent agreement with a theoretical χ^2 distribution for two degrees of freedom.

---

*Present address: Los Alamos Scientific Laboratory, Los Alamos, New Mexico 87545.
†Present address.

[1]F. E. Low, Phys. Rev. 110, 974 (1958).
[2]T. Burnett and N. Kroll, Phys. Rev. Lett. 20, 86 (1968).
[3]B. M. K. Nefkens and D. I. Sober, Phys. Rev. D 14, 2434 (1976).
[4]E. M. Nyman, Phys. Rev. 170, 1628 (1969).
[5]H. W. Fearing, Phys. Rev. C 6, 1136 (1972).
[6]H. W. Fearing, in *Nucleon-Nucleon Interactions—1977*, Proceedings of the Second International Conference on Nucleon-Nucleon Interactions, Vancouver, 1977, edited by D. Measday, H. Fearing, and A. Strathdee (AIP, New York, 1978); and to be published.
[7]D. Sober, M. Arman, D. Blasberg, R. Haddock, K. Leung, B. Nefkens, B. Schrock, and J. Sperinde, Phys. Rev. D 11, 1017 (1975).
[8]K. Leung, M. Arman, H. Ballagh, P. Glodis, R. Haddock, B. Nefkens, and D. Sober, Phys. Rev. D 14, 698 (1976).
[9]B. M. K. Nefkens, M. Arman, H. Ballagh, P. Glodis, R. Haddock, K. Leung, D. Smith, and D. Sober, Phys. Rev. D 18, 3911 (1978).
[10]L. M. Lederman, in *Proceedings of the 1975 International Symposium on Lepton and Photon Interactions at High Energies, Stanford, California*, edited by W. T. Kirk (SLAC, Stanford, 1976), p. 265.
[11]R. Rückl, Phys. Lett. 64B, 39 (1976).
[12]E.g., Review by M. L. Halbert, in *Proceedings of the Gull Lake Symposium on the Two-Body Force in Nuclei, Gull Lake, Michigan, 1971*, edited by S. M. Austin and G. M. Crawley (Plenum, New York, 1972); J. V. Jovanovich, in *Nucleon-Nucleon Interactions—1977*, Ref. 6, p. 451; J. Beveridge *et al.*, *ibid.* p. 446.
[13]O. Chamberlain, private communication.
[14]D. I. Sober, M. Arman, D. J. Blasberg, R. P. Haddock, K. C. Leung, and B. M. K. Nefkens, Nucl. Instrum. Methods 108, 573 (1973).
[15]B. M. K. Nefkens, O. R. Sander, and D. I. Sober, Phys. Rev. Lett. 38, 876 (1977).
[16]B. M. K. Nefkens, in *Nucleon-Nucleon Interactions—1977*, Ref. 6, p. 477.
[17]B. A. Ryan, A. Kanofsky, T. J. Devlin, R. E. Mischke, and P. F. Shepard, Phys. Rev. D 3, 1 (1971).
[18]P. Signell, in *Advances in Nuclear Physics*, edited by M. Baranger and E. Vogt (Plenum, New York, 1969), Vol. 2, p. 223.
[19]J. S. Bell and R. Van Royen, Nuovo Cimento 60A, 62 (1969).
[20]H. W. Fearing, Phys. Rev. D 7, 243 (1973).
[21]M. H. MacGregor, R. A. Arndt, and R. M. Wright, Phys. Rev. 169, 1149 (1968).
[22]H. B. Willard *et al.*, Phys. Rev. C 14, 1545 (1976).
[23]R. J. Cence, D. L. Lind, G. D. Mead, and B. J. Moyer, Phys. Rev. 131, 2713 (1963).
[24]A. Szyjewicz and A. N. Kamal, in *Nucleon-Nucleon Interactions-1977*, Ref. 6, p. 502; also, Contributions to Eighth International Conference on Few Body Systems and Nuclear Forces, Graz, 1978 (unpublished).
[25]L. Tiator, H. J. Weber, and D. Drechsel, Nucl. Phys. A306, 468 (1978).
[26]A. N. Kamal and A. Szyjewicz, Nucl. Phys. A285, 397 (1977).
[27]R. Rückl, private communication.